Dynamics of retinal photocoagulation and rupture

Christopher Sramek
Stanford University
Department of Applied Physics
452 Lomita Mall, Room 140
Stanford, California 94305

Yannis Paulus
Stanford University
Stanford University School of Medicine
452 Lomita Mall, Room 137
Stanford, California 94305

Hiroyuki Nomoto
Stanford University
Department of Ophthalmology
300 Pasteur Drive, Room A22
Stanford, California 94305

Phil Huie
Stanford University
Department of Ophthalmology
452 Lomita Mall, Room 136
Stanford, California 94305

Jefferson Brown
Stanford University
Department of Physics
452 Lomita Mall, Room 137
Stanford, California 94305

Daniel Palanker
Stanford University
Department of Ophthalmology
    and
Hansen Experimental Physics Laboratory
452 Lomita Mall, Room 135
Stanford, California 94305

Abstract. In laser retinal photocoagulation, short (<20 ms) pulses have been found to reduce thermal damage to the inner retina, decrease treatment time, and minimize pain. However, the safe therapeutic window (defined as the ratio of power for producing a rupture to that of mild coagulation) decreases with shorter exposures. To quantify the extent of retinal heating and maximize the therapeutic window, a computational model of millisecond retinal photocoagulation and rupture was developed. Optical attenuation of 532-nm laser light in ocular tissues was measured, including retinal pigment epithelial (RPE) pigmentation and cell-size variability. Threshold powers for vaporization and RPE damage were measured with pulse durations ranging from 1 to 200 ms. A finite element model of retinal heating inferred that vaporization (rupture) takes place at 180–190°C. RPE damage was accurately described by the Arrhenius model with activation energy of 340 kJ/mol. Computed photocoagulation lesion width increased logarithmically with pulse duration, in agreement with histological findings. The model will allow for the optimization of beam parameters to increase the width of the therapeutic window for short exposures. © *2009 Society of Photo-Optical Instrumentation Engineers.* [DOI: 10.1117/1.3130282]

Keywords: photocoagulation; damage threshold; computer model; retinal pigment epithelium; retinal thermal damage.

1 Introduction

Argon laser photocoagulation has long been the standard of care for several retinopathies.[1–4] Laser pulse durations have typically been in the range of 100–500 ms, with spot sizes varying from 50 to 500 μm. Although successful in coagulating the photoreceptor layer, pulses of these durations are known to produce collateral thermal damage to the inner retina.[5] Patterned scanning laser photocoagulation, a new method of retinal phototherapy, departs from these traditional parameters by using a scanning laser to apply patterns of 4 to 50 lesions, with pulse durations in the range of 10–30 ms.[6] The number of pulses applied in each pattern is limited by the eye fixation time—on the order of half a second. Clinical studies have shown that this regime is less painful and as efficacious as traditional retinal photocoagulation, reported to date over short periods of follow-up.[5,7] Moreover, short-duration pulses appear to target the photoreceptor layer more selectively, reducing unintended damage to the neural retina.[8] However, shorter pulses require higher peak powers and retinal temperatures for coagulation, thus increasing the potential for photomechanical injury and rupture of Bruch's membrane.[9] Consequently, it has been observed that the safe therapeutic window (defined as the ratio of threshold powers for rupture and mild retinal coagulation) decreases with decreasing pulse duration. The safe therapeutic window for 10-ms pulses has been reported to be between 2.5 and 3, showing an increase for larger spot sizes.[10]

Photocoagulation with shorter pulses enables an increase in the number of lesions in a pattern applied during a single treatment and improves spatial confinement of the thermal

Address all correspondence to: Christopher Sramek, Applied Physics, Stanford University, 452 Lomita Mall-Room 140 Stanford, California 94305; Tel: 650–723–0130; Fax: 650–725–8311; E-mail: csramek@stanford.edu

spread in the retina. At the same time, pigmentation in human eyes varies by about a factor of 2,[11,12] and the safe therapeutic window should not be smaller than this.[10] In order to balance these considerations, it is useful to understand the dynamics of retinal photocoagulation and rupture, as well as the factors that determine the thresholds of these processes. Thermal modeling can play an important role in furthering this understanding, as it provides a quantitative estimate of temperature elevation within the retina during the laser pulse. Coupling heat conduction and thermal damage models allows for the prediction of damage zone size for arbitrary laser parameters. This enables calculation of the number of lesions required for different treatment parameters to affect the same total area of the retina, which is an important factor for clinical efficacy. It also provides guidance for optimization of the laser parameters in order to improve safety of photocoagulation at shorter pulses.

Several thermal models for retinal photocoagulation have been previously developed.[13–18] These numerically or analytically solve the heat conduction equation and estimate the extent of damage using the Arrhenius rate process model for cellular death.[15,19,20] Although these models agree with experimental photocoagulation data, few investigate the subject of retinal hemorrhage in the millisecond time regime. This process is essential for describing the safety limits of photocoagulation, and it is important that the relevant underlying parameters are understood if short-duration pulses are to be used clinically.

For accurate prediction of spatial damage extent in the retina and the width of the safe therapeutic window, it is desirable to use experimentally verified parameters in a numerical model. To this end, several important model parameters require further characterization: bulk absorption coefficient of the retinal pigmented epithelium (RPE), non-uniformity in RPE pigmentation, size distribution of RPE cells, and beam shape *in vitro* and *in vivo*. In addition, Arrhenius damage model parameters should be inferred from cell viability measurements.

Localized variations in light absorption are of primary importance because they directly influence temperature rise during the laser pulse. Correct assessment of the absolute temperature in each retinal layer is essential for two reasons. First, the Arrhenius damage model describes cell death rate as a strong function of temperature; therefore, small changes in temperature have a large impact on the extent of damage. Second, photomechanical injury or rupture occurs when interstitial water is vaporized, resulting in vapor bubble expansion.[21] Estimation of temperature at vaporization threshold in the retina provides a means of calibrating the model parameters.

Nonuniformity in heat deposition may arise from a variety of sources. First, any coherent beam will have some spatial irradiance fluctuations due to speckling. In addition, localized variations in RPE pigmentation result from the heterogeneous distribution of melanosomes across the RPE cell and between cells.[22] The degree of nonuniformity in RPE pigmentation has been found to vary between species and as a function of position in the fundus, with reported variations as high as a factor of 3 from macula to periphery.[23] Finally, variations in choroidal vascularization produce visible striations in pigmentation. These sources of nonuniformity can result in the for-

mation of "hotspots," areas with higher peak temperature, which can play a critical role when considering vaporization thresholds.

The Arrhenius model of cellular thermal damage is based on the following assumptions:[24,25] (*i*) the existence of a critical component of cellular metabolism with lowest heat tolerance, (*ii*) a description of the denaturation of this component in terms of chemical reaction theory, and (*iii*) an absence of cellular repair during the period of hyperthermia. In this approximation, one expects that cells will tolerate the same total amount of damage independent of heat pulse length, where damage is defined as a decrease of the critical component concentration. This total damage can be calculated by integrating the temperature-dependent reaction rate during the heat pulse. In the Arrhenius approximation, a decrease in concentration of a chemical component D can be expressed as[25]

$$dD(t) = -D(t)A \exp\left(-\frac{E^*}{RT(t)}\right)dt, \qquad (1)$$

where $D(t)$ is the current concentration, A is the reaction rate constant (in liter per second), E^* is the reaction excitation energy (in joules per mole), R is the universal gas constant (8.31 J/mol K), and T is the absolute temperature (in Kelvin). The criterion for cell viability can then be determined as a maximum tolerable decrease in concentration of the critical chemical component ($D_{threshold}/D_0$), which can then be written as[25]

$$\Omega = A \int_0^\tau \exp\left(-\frac{E^*}{RT(t)}\right)dt = -\ln\left(\frac{D_{threshold}}{D_0}\right) \qquad (2)$$

where τ is the duration of hyperthermia, including both heating and cooling phases. Although the exact value of the damage integral Ω corresponding to cell death is not known, it is usually assumed to be equal to 1,[26] which means that the concentration of the critical component is reduced by a factor of e. There have been other reports claiming that cells will not survive if even 5–10% of a critical protein is denatured.[27] Selection of the value for the damage integral will affect the value of the rate constant A deduced from experimental data, but it will not affect the value of E^*. For simplicity, the damage integral was assumed to be equal to 1 in this study.

Protein activation energies have been measured to vary from 200 to 800 kJ/mol.[15] Damage to porcine cornea has been described with an activation energy of 106 kJ/mol,[28] while cultured NIH3T3 cells were estimated to have an activation energy of 96 kJ/mol.[25] In retina, Vassiliadis inferred an activation energy of 290 kJ/mol from millisecond argon laser lesions, a value which has been commonly used in retinal damage models.[29]

In this work, we performed an independent assessment of this damage model parameter for retinal coagulation, along with measurements of laser transmission through the ocular tissues, and nonuniformity of absorption in RPE. Together, this allowed for the construction of a finite element thermal damage model and the prediction of lesion width for various treatment parameters.

2 Materials and Methods

2.1 Laser System

A single laser system was used throughout this work. A PAS-CAL photocoagulator (Optimedica, Santa Clara, CA) provided optical radiation from a continuous wave (CW) frequency-doubled (532 nm) Nd:YAG laser. The photocoagulator consists of a modified slit lamp and optical system, which telecentrically images the surface of a multimode step index optical fiber through a two-axis scanner. Peak output power can be continuously varied from 10 to 2500 mW. A graphical user interface allows clinical parameters including spot size, duration, and power to be controlled, and a foot pedal activates the laser. This system was used to produce pulses of $1-200$ ms in duration with a 200-μm spot size in the aerial focal plane.

2.2 RPE Cell Absorption and Size Distribution

RPE sheets were extracted from three Dutch-belted rabbit eyes <20-min postenucleation. Square sections of posterior pole were removed from each eye, and the retina and RPE were peeled off the choroid, with large sheets ($\sim$4 mm^2) of RPE adhering to the photoreceptors. The retinas with adherent RPE were placed in fixative for 1 h and examined with transmission microscopy. A 563-nm wavelength LED (model no. B4303F5, CML Innovative Technologies, Inc., Hackensack, New Jersey) was used for illumination. High-resolution images of RPE cells were acquired with a CCD camera (Micropublisher 3.3; Qimaging Inc., Surrey, BC). A dark reference level for subsequent absorption analysis was obtained by placing a 50-μm metal wire in the sample plane. The resulting images were evaluated with the *ImageJ* software package (1.37v, NIH, Bethesda, Maryland) to estimate cell-to-cell variation in RPE absorption.[30] To assess the size distribution of the RPE cells, a grayscale threshold was applied to each image to outline the boundaries between the pigmented regions ($N=1623$ regions total). Area and mean green channel grayscale values for each fitted region were recorded. Separately, the transmittance of the near-collimated 532-nm laser was measured through the same RPE samples to provide a second estimate of cellular absorption.

2.3 Vaporization Delay in RPE Sheets

Transmitted and backscattered laser light during the irradiation of RPE cells was monitored using the optical setup shown in Fig. 1. A 10-kHz bandwidth large area photodiode (model no. 2031; New Focus, Inc., San Jose, California) measured the light pulse transmitted through the sample, while a second photodiode (DET410, Thorlabs, Inc., Newton, New Jersey), measured the backscattered light. Photodiode signals were recorded simultaneously on a digital oscilloscope (TDS1001B, Tektronix, Inc., Beaverton, Oregon).

RPE explants were prepared from freshly enucleated porcine eyes, shipped on ice overnight. Eyes were cut equatorially, and the anterior pole and vitreous were removed. Square samples roughly 15 mm in width were prepared from the posterior segment of each eye. The retina was carefully removed, exposing the undamaged RPE. Because of the long delay (roughly 24 h) between enucleation and retinal peeling, the retina was detached from the RPE and its peeling did not
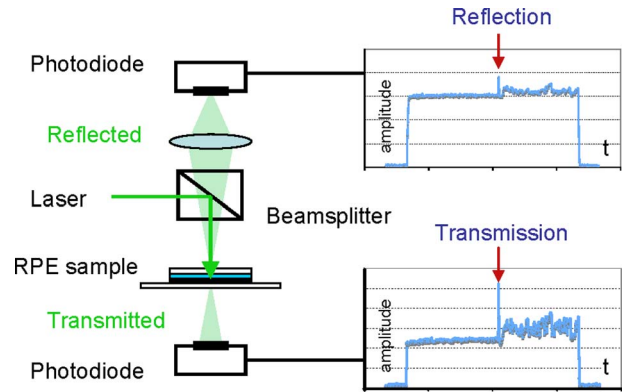

Fig. 1 Diagram of the experimental setup for the vaporization delay measurements. Incident powers between 160 and 640 mW were used. Delay was measured between the pulse onset and the first peak maximum.

damage the underlying cells. Samples were placed in a Petri dish, irrigated with PBS, and covered with a microscope cover glass.

Irradiation was performed with the laser at six powers ranging from 160 to 640 mW. The backscattered and transmitted light pulses recorded by the photodiodes were evaluated for characteristic peaks corresponding to bubble formation (indicated by arrows in Fig. 1). Laser pulse duration was initially adjusted for each power to ensure a bubble formation signal was consistently observed by at least one of the photodiodes. Durations varied between 3 ms at 640 mW and 200 ms at 160 mW. At each power, roughly 550 vaporization peaks were observed, and the time delay between pulse onset and transmission or reflection peak was recorded for each event. Measurements were made in 11 eyes, totaling 3300 exposures. To verify that optical scattering peaks corresponded to bubble formation, a hydrophone was used to detect acoustic transients. Acoustic signals coincided with the optical scattering peaks, confirming that explosive vaporization was the origin of the optical signals.

2.4 In-Eye Beam Characteristics

An optical system was constructed to measure the beam shape and power at the retinal plane, similar to Birngruber et al.[31] One eye was enucleated from each of three rabbits, one Dutch belted and two New Zealand whites. A 4-mm-diam window was cut through the sclera, choroid, and retina in the macular region. A microscope glass cover slip was glued over the hole in the posterior pole. An ocular contact lens (OMSRA-S; Ocular Instruments, Bellevue, Washington) was used to focus the laser beam through the central cornea onto the cover slip. A transparency with a printed 300-μm pitch grid placed on the cover slip served as a target for focusing the laser and calibrating the beam images. A $10\times$ imaging objective lens was used to magnify the beam in the retinal plane onto a CCD (Micropublisher 3.3; Qimaging Inc., Surrey, BC) and a power meter head (PD-300; Ophir Optronics Ltd, Jerusalem, Israel). In addition, an iris was used to restrict the imaging and power measurements to a 500-μm diameter in the retinal plane. Measurements were taken <30-min postenucleation to minimize the effects of corneal edema.

2.5 RPE Viability Thresholds

Seven Dutch belted rabbits were used in accordance with the Association for Research in Vision and Ophthalmology Resolution on the Use of Animals in Ophthalmic and Vision Research with approval from the Stanford University Animal Institutional Review Board. The rabbits were anesthetized using ketamine hydrochloride (35 mg/Kg), xylazine (5 mg/Kg), and glycopyrrolate (0.01 mg/Kg). Pupil dilation was achieved by 1 drop each of 1% tropicamide and 2.5% phenylephrine hydrochloride, and topical tetracaine hydrochloride 0.5% was used for local anesthesia. A laser contact lens (OMSRA-S; Ocular Instruments, Bellevue, Washington) was placed onto the mydriatic eye using hydroxypropyl methylcellulose as a contact gel.

Ophthalmoscopically visible marker lesions were used in all eyes to provide orientation during sample evaluation. Three sets of marker lesions were placed adjacent to the medullary ray, oriented parallel to each other, and spaced ~2 mm apart. Test exposures were placed in columns between these marker lesions, and both test and marker exposure locations were documented graphically. Approximately 50 test exposures were placed in each eye. The first exposures always produced ophthalmoscopically visible lesions and stepwise decreases in power led to ophthalmoscopically invisible results. Pulse durations of 1–200 ms were used, with each column of test exposures corresponding to a single duration. In total, roughly 50 exposures were placed for each duration. Taking into account the combined magnifications of the rabbit eye and contact lens of 0.66, the aerial beam diameter of 200 μm approximately corresponded to a retinal spot size of 132 μm.[32]

The animals were sacrificed with a lethal dose of IV Beuthenasia in the marginal ear vein, and the eyes were enucleated <10 min later. The globes were cut equatorially, and the anterior part and vitreous humor were removed. Square samples of roughly 10 mm in width were prepared from the posterior segment of each eye. The neural retina was carefully removed to expose the RPE while preventing RPE adhesion to the retina. Samples of posterior segment were placed in a Petri dish and stained with an Ethidium homodimer 1 (EthD-1) solution. Dead cells fluoresce red because the dye penetrates damaged cellular membranes, binds to nucleic acids, and undergoes an enhancement of fluorescence.[33] Staining took place no more than 20 min after enucleation. Cell viability was assessed based on fluorescence images taken with a digital camera, 20 min after staining, when fluorescence reached its maximum level. Images were evaluated using *ImageJ*, and diameter of the damaged zone was measured in each lesion.

2.6 Thermal Model

2.6.1 Geometry

Axisymmetric models of the porcine RPE explant and rabbit posterior pole were constructed in the finite element computational package COMSOL 3.4.[34] The porcine explant model [Fig. 2(a)] included two homogenous absorbing layers, the RPE and choroid. On the basis of porcine retinal histology, the pigmented layer formed by melanosomes in the RPE was assumed to be 4 μm in thickness, and choroidal thickness was estimated to be 70 μm. The rabbit *in vivo* model [Fig.
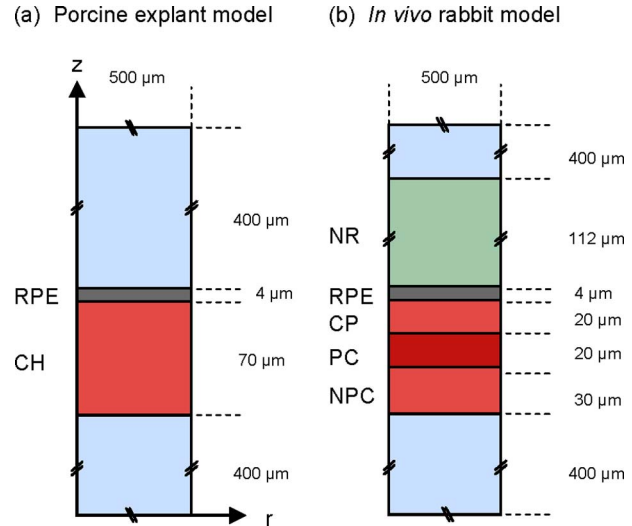

Fig. 2 (a) Geometry of the porcine explant model for COMSOL computations. Two absorbing layers were assumed: 4 μm thick RPE and 70 μm choroid (CH). (b) Geometry of the *in vivo* rabbit retina model. Absorbing layers are neural retina (NR), RPE, choriocapillaris (CP), pigmented choroid (PC), and nonpigmented choroid (NPC). Absorption and scattering coefficients are given in Table 1.

2(b)] was made up of five superposed absorbing layers, summarized in Table 1. Layer thicknesses were estimated from histology and from previously reported values for rabbit in the literature.[16] In addition to absorbing regions in the neural retina, RPE, and choriocapillaris, a 20-μm-thick region of higher pigmentation in the choroid located 40 μm below the RPE was assumed.[15] The computational domain was extended 500 μm radially and included a 400-μm nonabsorbing layer above and below the first and last absorbing layers. Scleral absorption was neglected.

2.6.2 Heat conduction equation

Calculation of laser-induced heating in both models was performed by solving the transient heat conduction equation:

$$\rho c_p \frac{\partial T}{\partial t} = \nabla(k \nabla T) + Q(r,z,t) \qquad (3)$$

where ρ and c_p are the density and heat capacity of the medium, k is the thermal conductivity, and Q is the volumetric heat source term, dependent on optical absorption in the modeled layers. The temperature-dependent thermophysical properties of liquid water were used for all layers.[35]

Convective cooling due to choroidal blood perfusion in the *in vivo* case can be estimated with an additional heat loss term,

$$Q_{\text{perfusion}} = -A_{\text{perfusion}}\rho_{\text{blood}}c_{\text{blood}}(T - T_o) \qquad (4)$$

where $A_{\text{perfusion}}$ is the local perfusion rate, ρ_{blood} and c_{blood} are the density and heat capacity of blood, and T_o is the arterial temperature, assumed to be the same as the baseline body temperature, 37 °C. Perfusion rates for the choriocapillaris and choroid were taken from literature to be A_{CPL}=2.4 s^{-1} and A_{CHD}=0.3 s^{-1}.[16] Comparison of results with no convection showed less than a 1% difference in peak temperature

Table 1 Optical properties of absorbing ocular tissues at 532 nm. Layer thicknesses were taken from literature and estimated from histology.[15,16] Absorption and scattering coefficients were determined from experiments (Section 3.2) and literature.[15,39]

Tissue	Thickness $\Delta z (\mu m)$	Absorption $\mu_a (1/\text{cm})$	Scattering $\mu_s (1/\text{cm})$	Anisotropy factor g	$(1-g)\mu_s$ $(1/\text{cm})$
Neural retina	112	4.2	340	0.97	10
RPE	4	1400	1100	0.84	180
Choriocapillaris	20	160	740	0.87	96
Pigmented choroid	20	1400	740	0.87	96
Nonpigmented choroid	30	160	740	0.87	96

rise for 200-ms exposures. This finding confirmed that the temperature rise was practically unaffected by blood perfusion due to the short duration of the exposures, as suggested by a previous study.[36] Perfusion was thus not included in the final computations. Other hydrodynamic convective cooling processes, such as vitreous flow, have been shown to be insignificant over the relevant time scales.[18]

2.6.3 *Heat deposition*

Heat deposition in the absorbing layers was calculated based on measured irradiance profiles and absorption coefficients determined from literature and experiments. For the RPE explant model, the aerial radial irradiance profile of the laser beam was fit with an error function

$$\Phi(r) = \Phi_0 \left[1 + \text{erf}\left(\frac{a-r}{b} \right) \right] \quad (5)$$

where a and b are fit parameters and Φ_0 is the peak irradiance. The experimental beam profile and the fit function are plotted in Fig. 3(a). The irradiance distributions shown were normalized to yield the same total incident laser power. The same function was fit to the measured in-eye beam profile for the *in vivo* rabbit model.

Absorption of laser radiation in non-scattering medium is described by the Beer–Lambert law, with the heat source term given by

$$Q(r,z) = \mu_a(z)\Phi(r)\exp(-\mu_a z) \quad (6)$$

where $\mu_a(z)$ is the absorption coefficient within a layer. Micrometer-sized melanin granules are the primary absorbers distributed in the RPE.[15] The thermal relaxation time for such granules is on the order of 1 μs (i.e., at least three orders of magnitude shorter than the laser exposures used in these experiments). This justifies the assumption of homogeneous pigment distribution across the RPE cell. In practice, scattering also affects the irradiance and, in highly scattering media, the heat source can be described according to the Kubelka–Munk theory,

$$Q(r,z) = \mu_a(z)\Phi(r)\exp\{-[\mu_a + (1-g)\mu_s]z\} \quad (7)$$

where $\mu_s(z)$ is the layer scattering coefficient and g is the anisotropy factor.[37,38] Ocular tissue is highly forward scatter-

ing, satisfying the major assumption of the Kubelka–Munk theory. In the interest of accurately estimating the fluence at each layer, tissue scattering was incorporated in the computational models.

Absorption coefficients were determined from literature and experiment. In agreement with the transmission micros-
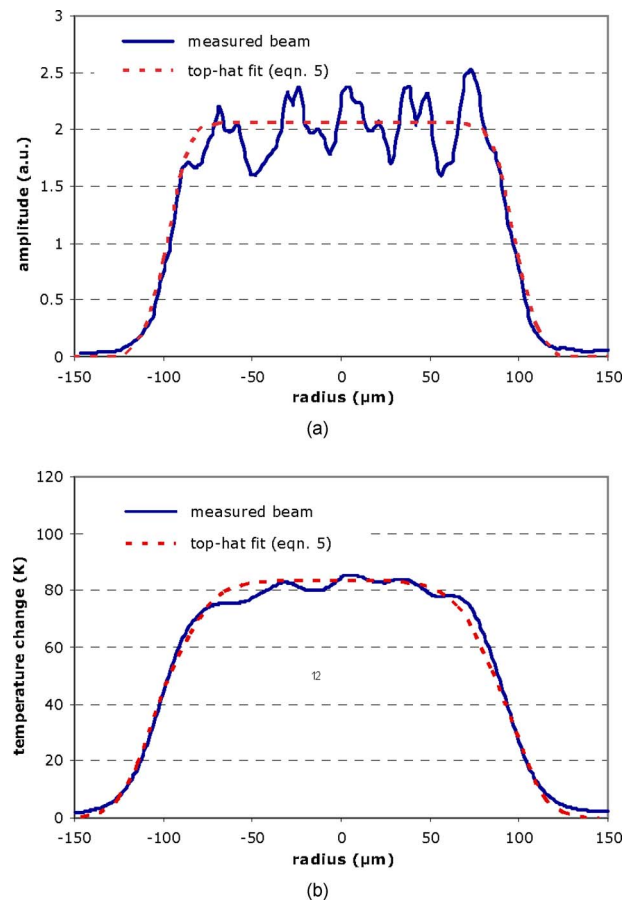

(a)

(b)

Fig. 3 (a) Measured PASCAL beam cross section and analytical function fit from Eq. (5). (b) Temperature change in the RPE layer corresponding to the measured and fit beam profiles for a 1-ms, 400-mW exposure. A simplified 3-D model consisting of a single absorbing layer ($\mu_a = 1600\text{cm}^{-1}$, thickness 4$\mu$m) in water was used with the nonaxisymmetric measured irradiance profile.

copy and bulk transmission measurements (Section 3.2), an RPE absorption coefficient of 1400 cm^{-1} was used. Porcine RPE was assumed to have similar bulk absorption and pigmentation variability as rabbit RPE, and porcine choroidal absorption was taken from previous measurements in that species.[39]

In rabbit, absorption coefficient of pigmented choroid was taken to be the same as the RPE. Remaining absorption coefficients for the rabbit model were those reported in the literature.[15,39] Retinal blood content in postmortem holangiotic bovine eyes (used in Ref. [39]) was assumed to be similar to the merangiotic rabbit retina in the model, as optical attenuation in the neural retina is dominated by scattering in either case. Scattering and anisotropy coefficients were taken from *in vitro* results reported by Hammer et al.,[39] which used double-integrating sphere measurements and inverse Monte Carlo simulations to infer these quantities for porcine and bovine retinal tissue. Absorption and scattering parameters for each retinal layer are summarized in Table 1.

2.6.4 *Finite element numerical solution*

The axisymmetric model geometry required the imposition of a zero heat flux boundary condition on the symmetry axis. The computational domain had a radius of 500 μm and a 400 μm axial span above and below the nearest absorbing layer, as shown in Fig. 2. Constant temperature was assumed on the external boundaries. However, the zero heat flux assumption resulted in the same temperatures. This is due to the fact that the region of significant temperature elevation beyond the laser beam for the longest pulse durations ($\sim$100 μm for a 200-ms exposure) was much smaller than the boundaries of the computational domain ($\sim$500 μm radius). In this limit, the domain behaves because infinite and boundary conditions do not play a significant role.

The described geometries were constructed in COMSOL 3.4 and finite element meshes of $\sim$5000 triangular elements were generated.[34] The heat conduction equation was solved using finite element method with UMFPACK, a direct linear system solver. The independence of the solution on the mesh size was checked by increasing the number of the mesh elements by 100%. The resulting peak temperature agreed with the solution for the coarser mesh within 1%.

As outlined above [Eq. (2)], the Arrhenius model describes tissue damage as an integral of the reaction rate over the period of hyperthermia. Further derivations and descriptions of the rate process model can be found in many previous studies.[15,19,20,24] The values of E^* and A for the RPE were determined using the computed temperature time courses from the RPE viability measurements. The Arrhenius integral was computed in all locations in the retina using the interpolated temperature time courses with trapezoidal integration.

3 Results

3.1 *Temperature Variation Due to Speckling*

At the image plane of the slit lamp microscope, the irradiance distribution of the 200-μm laser beam had a nominally top-hat profile with the transition from 10 to 90% occurring over roughly 20 μm. The experimental beam profile and its fit with an error function [Eq. (5)] are plotted in Fig. 3(a). Irra-
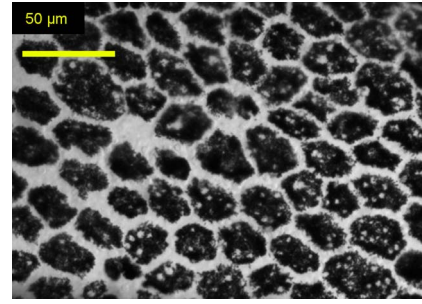

Fig. 4 Transmittance micrograph of rabbit RPE sheet taken at 563-nm wavelength. To measure cell sizes, the images were binarized by defining a gray-scale threshold value, 35% of the white level C_{white}. Pigmented regions were defined with the *ImageJ* particle analysis utility, which outlines objects and provides statistics for these regions.

diance fluctuations due to speckling were approximately $\pm$20%. With pulse duration of 1 ms, these fluctuations were calculated to produce only small variations in local peak temperature, on the order of 5% [Fig. 3(b)]. With longer pulses, these temperature fluctuations are even smaller.

3.2 *RPE Pigmentation Variability*

A sample micrograph of the rabbit RPE preparation under 563-nm LED illumination is shown in Fig. 4. The boundaries of the pigmented regions were outlined based on thresholding fits using *ImageJ*. Areas of the regions were quantified, and the equivalent cell diameters were computed. To quantify cell-to-cell variations in absorption, the mean green channel grayscale value C_{cell} for each fitted region was measured. The grayscale value of a "hole" (missing cell) in the RPE was taken as a white reference level C_{white}, while the grayscale value of the metal wire placed over the sample was taken as a black reference level C_{black}. As the sample was transilluminated and the camera response was linear, the mean transmittance fraction through the cell T_{cell} can be calculated as

$$T_{cell} = \frac{C_{cell} - C_{black}}{C_{white} - C_{black}}. \tag{8}$$

Histograms of the equivalent RPE cell diameters and absorption coefficients (assuming a pigmented layer thickness of 4 μm) are shown in Fig. 5. The mean cell diameter was $\sim$22 μm, while the average cell transmittance was 0.25, giving an inferred mean absorption coefficient of 3600 cm^{-1}. To estimate homogeneous attenuation, mean grayscale value over the entire RPE sheet within each image was measured, giving a transmittance T_{RPE} of 0.51$\pm$0.06. This transmittance corresponds to a bulk attenuation coefficient of 1700$\pm$300 cm^{-1}. For a 200-μm-diam beam, a single cell of diameter 22 μm occupies 1.3% of the irradiated area, or represents 2.1% of the irradiated cells, assuming a packing fraction of 60%. The lowest 2.1% of all measured transmittance values [highlighted and indicated by vertical line in Fig. 5(a)] have a mean value of 0.09$\pm$0.01, corresponding to an attenuation coefficient of 6100$\pm$200 cm^{-1}. On average, one such "dark" cell within the beam diameter will have this attenuation coefficient, resulting in formation of a local "hotspot."
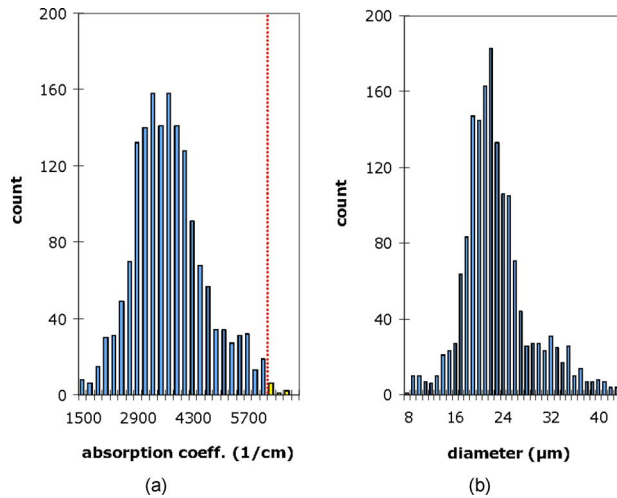
Fig. 5 Histograms of (a) cell absorption coefficient and (b) equivalent diameter (b), defined as $d = 2\sqrt{(A/\pi)}$, where A is the fit region area in micrometer squared. The largest 2.1% of absorption coefficients, corresponding to the "hot-spot" absorption used in the model, are indicated by the vertical line in (a).

Transmittance measurements of the near-collimated 532-nm laser beam through the same rabbit RPE samples yielded a mean transmittance of 0.60 ± 0.08, corresponding to a bulk absorption coefficient of 1300 ± 300 cm^{-1}. As opposed to the micrograph measurements based on Köhler illumination geometry, this second absorption measurement was more analogous to the irradiation conditions in our laser experiments. Larger angular spread in Köhler illumination enhances the contribution of scattering as compared to transmittance of the collimated laser beam. From Table 1, RPE scattering is expected to contribute 180 cm^{-1} to the total attenuation coefficient in the Kubelka–Munk approximation.[38] This component was subtracted from the hotspot and bulk attenuation coefficients inferred from microscopy, giving a single hotspot cell absorption coefficient of 5900 cm^{-1}. Homogeneous RPE absorption of 1400 cm^{-1} was used for the model, as a rounded average of the laser transmittance and scattering-corrected LED measurements.

3.3 Vaporization Delay

Time delays between pulse onset and vaporization in porcine RPE explants were measured for each of six laser powers, as shown in Fig. 6(a). The time delay for each power corresponds to a "threshold" pulse duration, where vaporization occurs at the end of the pulse. The solid line in Fig. 6(a) depicts an inverse-square-root dependence of power on threshold pulse duration. The threshold pulse durations and corresponding powers were used as input parameters for the numerical thermal model of the porcine RPE explants.

Calculated peak temperatures for these power/duration pairs are plotted in Fig. 6(b). The measured initial sample temperature of 24 °C was used as the baseline in the model. The use of a homogeneous RPE layer resulted in a decrease in the vaporization temperature at shorter pulse durations. Although such a trend is possible in situations where laser-induced pressure waves are present, the millisecond pulse durations were far outside the acoustic confinement regime.[40]
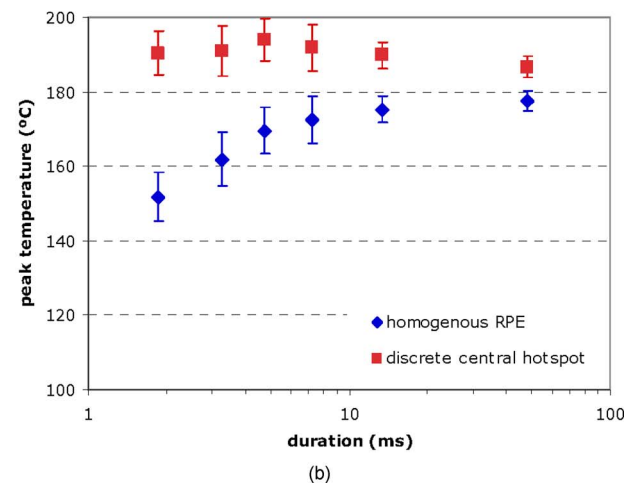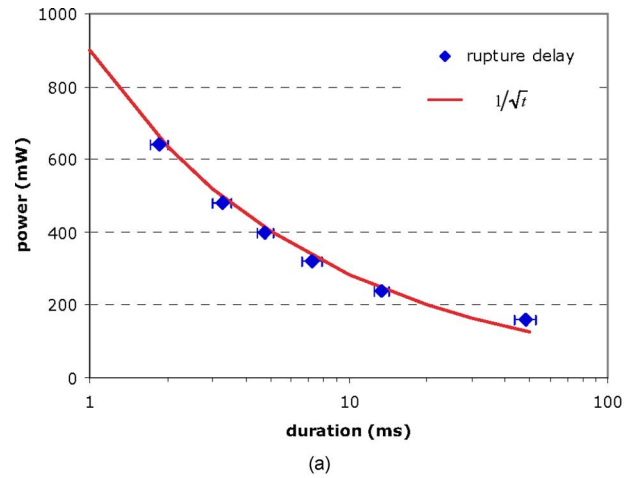

Fig. 6 (a) Incident laser power plotted as a function of measured time delay from pulse onset to vaporization in porcine RPE explant, and an inverse square-root fit (solid line). (b) Calculated peak temperatures in porcine explant model corresponding to threshold power/duration pairs with (■) and without (◆) a hot spot—a 22-μm-diam central area in the RPE with an absorption coefficient of 5900 cm^{-1}.

The addition of a single central hotspot with a higher absorption coefficient changes this dynamic. A region within the RPE layer of 11-μm radius and absorption coefficient $\alpha_{\text{hotspot}} = 5900$ cm^{-1} (as estimated above) raises the peak temperatures at shorter durations, giving a relatively constant vaporization temperature over the 2–50 ms range of pulse durations [Fig. 6(b)].

3.4 In-Eye Beam Characteristics and In Vivo Modeling

Typical results of the beam profile measurements in the enucleated rabbit eyes are shown in Fig. 7. A cross section of the beam in the retinal plane (solid line) is plotted along with a best-fit error function from Eq. (5) (dashed line). The dotted line depicts the expected profile from the aerial beam measurements, assuming a 0.66× demagnification by the combined refractive power of the contact lens and rabbit eye.[32] The beam appears to be demagnified further than expected, by a factor of 0.50× rather than 0.66×. The average measured FWHM diameter was 105 μm, with a 30–70% transition
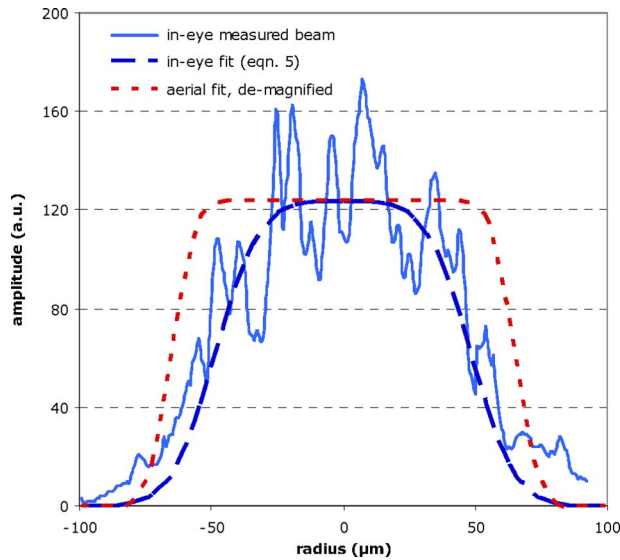
Fig. 7 Sample cross section of the measured in-eye beam shape (solid) and a fit from Eq. (5) (dashed). Aerial beam fit demagnified by 0.66x is also shown (dotted).

length of 22 μm. Ninety percent of the nominal laser power was incident on the cornea, with 69% transmitted through the 4-mm hole in the posterior pole. This implies an ocular media transmittance of 77%. However, only 41% of corneal power was measured within a 500-μm diameter in the retinal plane, indicating substantial scattering in the transparent ocular tissues.

The incorporation of the beam shape and power transmittance data along with rupture threshold data from earlier *in vivo* rabbit measurements[10] into the *in vivo* rabbit numerical model allows for computation of rupture threshold temperatures at various pulse durations. As can be seen in Fig. 8, the peak temperatures computed by the rabbit model are ~180°C, which is comparable to the values obtained in the experiments with porcine explants [Fig. 6(b)]. In contrast to the results based on the actual in-eye beam shape, the tem-
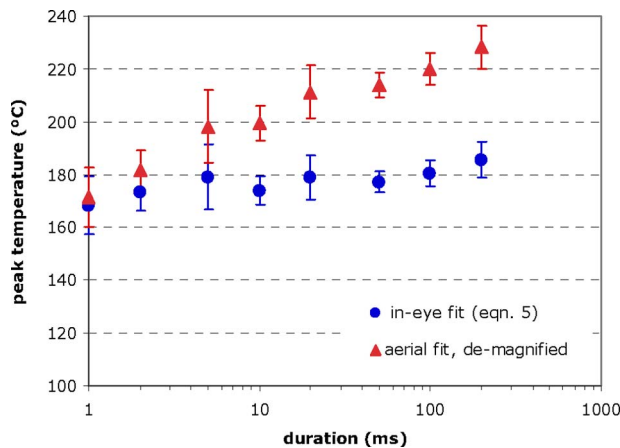

Fig. 8 Calculated peak temperatures in the rabbit *in vivo* model corresponding to rupture threshold powers from Ref. 10 [plotted in Fig. 9(a)]. Results corresponding to the 0.66× demagnified aerial beam shape (▲) and to the fitted in-eye beam shape (●) are plotted.

(a)

(b)

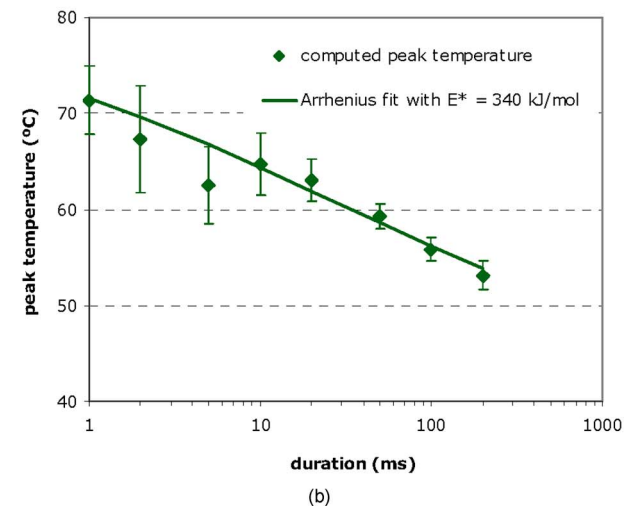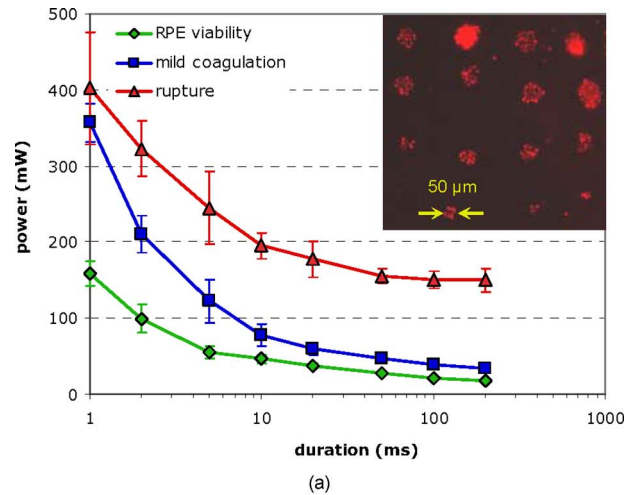**Fig. 9** (a) Threshold powers for RPE viability (♦), mild coagulation (■), and rupture (▲).[10] Inset: Fluorescent micrographs of an RPE sheet after staining with viability assay. A 50-μm threshold lesion diameter is indicated. (b) Peak temperatures corresponding to RPE viability thresholds, calculated at a 25-μm radius in the *in vivo* numerical model. Error bars correspond to the standard error in the viability threshold power measurements. Arrhenius fit with $E_* = 3.5$ eV is shown as a solid line.

peratures computed for a 0.66× demagnified fit of the aerial beam shape exhibit an increasing trend with longer exposures, which is unexpected for homogeneous absorption.

3.5 RPE Viability Thresholds

A sample image from the rabbit RPE viability threshold dataset is shown as an inset in Fig. 9(a). Lesion diameter was defined as the geometric mean of the vertical and horizontal widths. A 50-μm lesion diameter was used as a threshold, which corresponded to roughly six or seven cell clusters, making the laser lesions distinguishable from background solitary dead cells. The power to produce such a lesion at each pulse duration was recorded. Figure 9(a) shows the threshold power as a function of pulse duration, averaged over seven eyes. Also plotted are the threshold powers for mild coagulation and rupture.[10] Both the RPE viability and mild coagula-
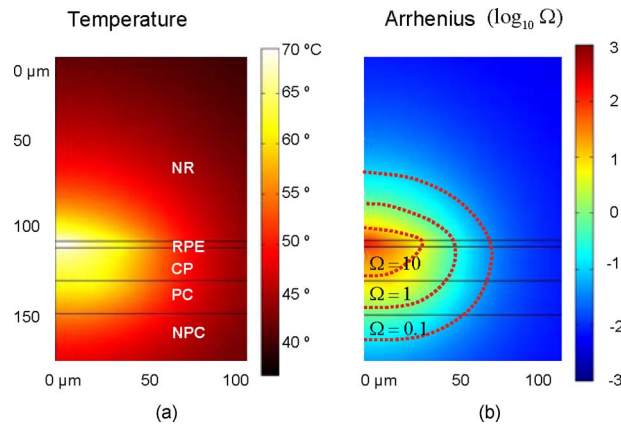
Fig. 10 (a) Peak temperature map corresponding to a 100-ms, 39-mW (mild coagulation threshold power) exposure. Absorbing layers are indicated as in Fig. 3. (b) $\log_{10}$ of Arrhenius integral with contours of constant value.

tion thresholds show an approximate $1/\tau^{1/2}$ dependence, with the viability threshold a factor of 2 lower for short durations.

The RPE viability threshold/duration pairs were used as input parameters to the *in vivo* thermal model. Temporal profiles of the temperature $T(t)$ at the top of the RPE layer at a distance of 25 μm from the center of the exposure were computed. Using these profiles for each duration, one can calculate damage integrals from Eq. (7), treating E^* as a time-independent constant. E^* can be varied and the least-squares method can be employed to find a value that gives a constant damage integral at all pulse durations and corresponding threshold powers for cell death. A value of $E^* = 340 \pm 40$ kJ/mol (3.5 ± 0.4 eV) was obtained in this manner. The rate constant corresponding to a damage integral $\Omega = 1$ was found to be $A = 1.6 \times 10^{55}$ s^{-1}.

Figure 9(b) shows the calculated peak temperatures reached at a 25-μm radius in the RPE for various pulse durations and corresponding experimental threshold powers. The continuous solid line depicts the computed peak temperatures achieved during pulses of various durations at powers necessary to yield the Arrhenius integral $\Omega = 1$ with the E^* and A values listed above. The Arrhenius model fits the experimental data well, within a range of uncertainty originating from the viability threshold measurements.

3.6 Estimating Lesion Diameter for Arbitrary Exposures

Assuming that all retinal cells have similar thermal sensitivity, the inferred activation energy E^* and rate constant A for the RPE can be used for all model layers. The extent of thermal damage can then be estimated for various laser parameters from Arrhenius integral contours. An example temperature map and corresponding Arrhenius plot for the rabbit model are shown in Fig. 10.

To validate the thermal damage model, a histological dataset of acute (enucleation <1 h post-treatment) retinal photocoagulation lesions was analyzed.[10] The maximum radial extent of histological damage at the RPE-outer segment interface was evaluated for 10–100-ms exposures with laser power varying from 50 to 250 mW. Damage was defined as
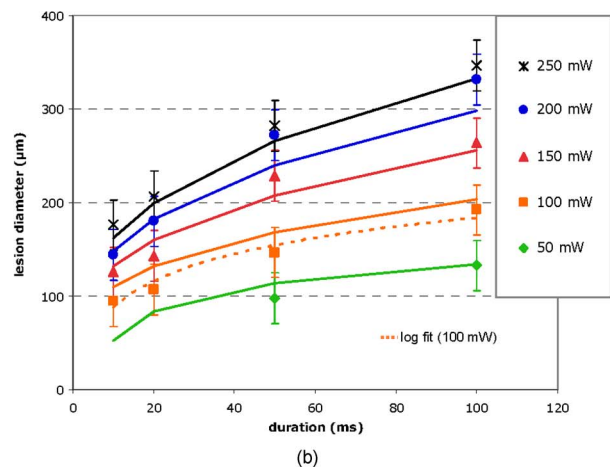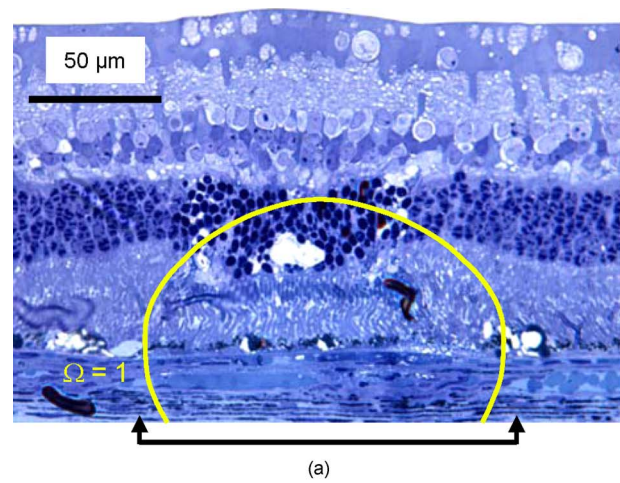

Fig. 11 (a) Circumference of the cellular damage zone (solid line) computed for a 10-ms, 150-mW pulse, overlaid on an acute histological section corresponding to the same treatment parameters. Note that the photoreceptors damaged within the yellow boundary exhibit pyknotic nuclei above the computed damage zone. Radial damage extent at the RPE-photoreceptor interface is indicated. (b) Histological (symbol) and model (solid line) lesion diameters as a function of pulse duration at several powers. Logarithmic fit to histological lesion diameter (dotted line) is shown for the 100-mW series. (Color online only.)

abnormal appearance of the photoreceptor outer segments, and estimated widths were averaged over two different lesions corresponding to the same laser parameters. Corresponding power/duration data pairs were used as input to the rabbit computational model. Damage zone width was computed as the diameter of the contour corresponding to an Arrhenius integral of unity at the top of the RPE layer.

A histological section from the dataset, with the computed damage zone boundary, is shown in Fig. 11(a). This example highlights some of the difficulties of estimating thermal damage extent in the retina. Both the primary thermal damage and the secondary reactive tissue changes are present, with only the primary thermal component described by the Arrhenius model. The secondary changes include pyknotic appearance of the nuclei in the inner nuclear layer and retinal edema. Pyknotic nuclei of the photoreceptors appear above the predicted damage zone since an entire cell is damaged if even only a part of the cell is inside the damage zone. To minimize

the secondary reactive changes, tissue was fixed for histology immediately (within 1 h) following the treatment. As these secondary reactive processes in the retina affect mainly the vertical (axial) extent of tissue damage, we consider the radial (lateral) extent at the RPE-photoreceptor junction to be a more reliable measure for comparison with the model.

Figure 11(b) shows a set of plots representing the experimental (symbol) and computed (solid line) lesion diameters as a function of duration and laser power. Error bars give conservative estimates of the uncertainty in the measured lesion width. Damage zone width appears to vary logarithmically with duration and linearly with power. The quantitative agreement between computed and histological lesion diameter indicates the applicability of the model to lateral extent of damage at the RPE-photoreceptor interface. However, the substantial uncertainty in the histological diameters and the imprecise estimation of axial damage [as in Fig. 11(a)] demonstrate the complex nature of retinal photocoagulation and the difficulty of making precise quantitative predictions.

4 Discussion

4.1 Heat Distribution and Vaporization in the RPE

Bulk absorption in the RPE is the primary factor determining temperature in the retina during photocoagulation and is hence critical to our model. Total rabbit RPE absorption in our measurements $(40 \pm 8\%)$ falls within the range typically cited in previous rabbit[15] and human[41] studies. In addition, our homogeneous absorption coefficient of 1400 cm^{-1} agrees well with values used in thermal modeling of the rabbit retina by Birngruber et al. (1560 cm^{-1} at 514 nm)[15] and measured for porcine eyes *in vitro* by Hammer et al. (1102 cm^{-1} at 527 nm).[39] In our rabbit model, pigmented choroidal absorption was taken to be the same as RPE, though one previous study used a value roughly 20% smaller.[15] This difference results in a minimal absorption increase ($\sim$4%) in the pigmented choroid, and an even smaller peak temperature increase ($<$1%) in the RPE.

Nonuniformity of heat deposition in the RPE plays an important role in retinal photocoagulation and rupture, particularly for shorter pulses. Significant variation in RPE pigmentation has been previously observed, with Pollack et al. attributing inconsistencies in the outcome of subvisible diode laser photocoagulation to pigmentation variability.[42] It has also been noted that in human and animal eyes, fundus pigmentation gradually changes from the macula to peripheral regions, with both melanosome density in individual cells and cell density contributing to this change.[43,44]

Inherent pigmentation variability within a beam diameter was inferred to have a significant influence on the peak temperatures computed from the vaporization delay measurements. With a homogeneous RPE, the numerical model predicted an increase in peak temperature with duration [Fig. 6(b)]. One explanation for this behavior is the presence of heat sources smaller than the beam size, which would increase peak temperature at shorter durations. In addition to pigmentation variability, irradiance fluctuations due to speckling were initially considered. However, a 3-D computational model showed that speckling produces temperature modulation of $<$5 °C [Fig. 3(b)], even for pulses as short as 1 ms. When RPE nonuniformity was taken into account in the form of a

central 22-μm hotspot with absorption coefficient 5900 cm^{-1}, the peak temperature at vaporization threshold increased to $\sim$190 °C and remained practically constant for pulse durations in the whole tested range, from 2 to 50 ms [Fig. 6(b)]. An alternative explanation for the calculated vaporization temperature increase in RPE explant at longer durations could be dynamic changes in RPE absorption. However, our transmittance measurements in porcine RPE explant showed near-constant transmittance until vaporization (Fig. 1) for all pulse durations.

Vapor bubble formation during nanosecond and microsecond exposures of the RPE has been extensively studied.[21,45–47] For these pulse durations, the heating is confined to individual melanosomes and a "vapor blanket" is formed when the melanosome surface reaches the vaporization threshold, estimated by Neumann et al. to be 157 ± 33 °C for microsecond pulses.[48] During millisecond pulses, heat diffuses tens of microns and the temperature distribution inside the RPE cell becomes near uniform. However, melanosomes are expected to remain acting as bubble nucleation sites. Computed temperatures at vaporization threshold (168–192 °C) in the current study fall in the upper end of the range measured with microsecond pulses.[48]

The primary focus of this model was the estimation of the cellular damage zone below the vaporization threshold; consequently, phase changes were not incorporated. Temperatures were calculated based on heat generation and conduction alone. It was assumed that vaporization begins at the hotspot when its temperature exceeds a threshold temperature, on the order of 180 °C for millisecond pulses. As soon as an initial bubble is created, the surrounding superheated water will start vaporizing into the growing cavity. Thus, the energy contributing to the bubble growth comes from a volume much larger than the hotspot itself, eventually corresponding to an area comparable to the final bubble diameter. For example, the latent heat necessary to create a 100-μm bubble is roughly 1 μJ, $\sim$1% of the energy absorbed in a 100-μm disk of RPE at the minimum rupture radiant exposure ($\sim$2 J/cm^2 at 1-ms duration). Nucleation temperature in water measured during pulsed electrical heating,[49] and CO$_2$ laser irradiation[25] varied $<$25% over the 1–100-ms range.

An interesting observation from the vaporization threshold measurements *in vitro* [Fig. 6(a)] and *in vivo* [Fig. 9(a) and Ref. 10] was the $1/\tau^{1/2}$ dependence of threshold power on pulse duration. One could explain such dependence assuming a presence of a single infinitely thin uniformly absorbing layer. A thin disk of radius R uniformly heated with power P will experience a temperature rise at its center proportional to[50]

$$\Delta T(\tau) \propto P\left\{\sqrt{\tau}\left(1 - e^{-(R^2/4D\tau)}\right) + \frac{R}{2\sqrt{D\pi}}\left[1 - \text{erf}\left(\frac{R}{2\sqrt{D\tau}}\right)\right]\right\},$$

(9)

where D is the thermal diffusivity of the surrounding medium. For $\tau < R^2/4D$ (17 ms for $R=100$ μm in water), ΔT scales as $P\tau^{1/2}$ and for fixed vaporization temperature, threshold power then scales as $1/\tau^{1/2}$. For heat sources of finite thickness, this heat conduction-dominated regime breaks down at pulse durations shorter than the time it takes for heat to dif-

fuse across the heat source. For a 4-μm-thick pigmented RPE, this duration is on the order of 10 μs. When heat diffusion during the laser pulse is negligible (thermal confinement condition) the threshold power varies as $1/\tau$ for constant temperature. The $1/\tau^{1/2}$ regime is also limited on the long-exposure end: at pulse durations $\tau \gg R^2/4D$, the first term in Eq. (9) becomes negligible as the temperature approaches a steady-state value. In this regime, the threshold power loses its dependence on pulse duration.

Despite the fact that a thin-disk model could explain the observed dependence, there are two additional factors in the retinal absorption: significant absorption in the choroid, and strong nonuniformity of the absorption coefficient in the RPE. Inclusion of choroidal absorption increases the volume of the heat source and slows down heat diffusion, resulting in increased peak temperature for longer exposures. On the other hand, stronger absorption in some of the RPE cells leads to higher computed threshold temperatures at shorter durations. These two effects counteract each other, yielding an overall $1/\tau^{1/2}$ dependence in the millisecond range.

Although the vaporization delay measurements on RPE explants highlighted the role of absorption nonuniformities in determining peak temperatures, the in-eye beam measurements highlighted another important aspect of retinal heat deposition: the effects of the transparent ocular tissues on transmittance and shape of the laser beam. Kidwell et al. measured an *in vivo* argon laser (514 nm) transmittance to the retina in rabbit eyes of $85 \pm 9\%$.[51] However, Birngruber et al. found only $51 \pm 9\%$ of the corneal laser power within the focal spot on the retina, attributing the loss to scattering in the anterior segment.[31] Ocular transmittance of $77 \pm 17\%$ in our measurements is consistent with Kidwell, while power reaching the focal area ($41 \pm 7\%$) is particularly low.

We observed an average beam demagnification of $0.53\times$ (FWHM) rather than the expected $0.66\times$ combined magnification of the contact lens and rabbit eye.[32] In addition to demagnification, the radial decrease of laser irradiance at the edges of the top-hat beam profile was slower compared to the demagnified aerial beam (Fig. 7). Corneal edema and minor mechanical deformations of the globe are possible sources of the observed small-angle scattering and beam distortions, but the precise origin remains to be investigated. With an assessment of power transmittance and beam shape in the eye, the computed temperatures were $\sim 180\,^\circ$C, close to the vaporization threshold obtained in our *in vitro* experiments.

4.2 Cellular Viability during Hyperthermia

The RPE viability thresholds shown in Fig. 9(a) for 1–200-ms durations correspond to peak radiant exposures of 2–44 J/cm². A similar range has been previously reported in RPE viability measurements in bovine RPE explants: 0.8–20 J/cm² for a comparable beam size (120 μm) and similar durations (1–100 ms).[13] Comparable thresholds have also been observed in porcine explants treated with a smaller beam (50 μm): RPE damage thresholds were 1.2 and 4.3 J/cm² for 0.5 and 3-ms durations, respectively.[21]

Computed peak temperature corresponding to our viability threshold powers decreased from 72 to 53 °C as pulse duration increased from 1 to 200 ms [Fig. 9(b)]. Previous measurements of cellular hyperthermia during prolonged expo-
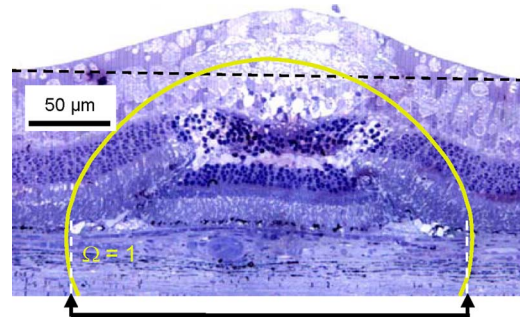

Fig. 12 Circumference of the cellular damage zone (solid line) computed for a 100-ms, 150-mW pulse, overlaid on an acute histology of an intense lesion, corresponding to the same treatment parameters. Note that the computed damage zone extends beyond the initial retinal thickness (dotted line), indicating full-thickness damage.

sures (>1 s) estimated threshold temperatures in the range of 40–55 °C.[26,27] Tissue temperature was also measured during retinal photocoagulation *in vivo* using microthermocouples.[52] With pulse durations varying from 20 ms to 10 s, the threshold temperature for producing a visible lesion decreased from 92 to 62 °C. This is significantly higher than our computed temperatures but is expected, because our RPE viability threshold power was measured to be 40–60% lower than that of visible coagulation [Fig. 9(a)].

Several previous studies have shown that thermal damage is the primary mechanism for RPE cell death in the millisecond range of pulse durations.[21,46] The Arrhenius model describing thermally induced cell death has been successfully applied to fit experimental data, but there are few published estimates of the Arrhenius activation energy and rate constant for retinal tissue.[13–15] The value of E^* inferred in the current study (340 kJ/mol = 3.5 eV) compares well to that of Vassiliadis (290 kJ/mol = 3.0 eV).[29]

In previous studies, thermal modeling was used to predict confinement of thermal damage to various retinal layers[8,15,18] and to correlate lesion size with reflectance of a probe laser.[53] The latter study also compared ophthalmoscopically measured lesion diameters to computed diameters at a single laser power. Figure 11(b) demonstrates that lesion diameters calculated in the current model show quantitative agreement with histological lesion diameters measured at the RPE-photoreceptor interface over a broad range of laser parameters. Secondary tissue changes make the quantitative comparison of axial retinal damage extent more difficult. However, the model can still make important qualitative predictions about the axial penetration of thermal damage, such as the extent of primary damage in various retinal layers.

Figure 12 shows a histological section of an intense lesion produced by a 100-ms, 150-mW pulse, overlaid with the calculated extent of primary thermal damage. It illustrates correlation with the model, as well as some limitations. Although significant edema is apparent, full-depth primary damage is both predicted and observed. Lesion width at the RPE-photoreceptor junction shows quantitative agreement with the model as in Fig. 11(a), but radial damage extent above the RPE deviates substantially. In computing Arrhenius damage contours, it is assumed that a single activation energy E^* applies to all retinal cells. Variations in thermal sensitivities

among cell types could explain the observed differences between predicted and measured damage extent in various retinal layers. Furthermore, in cases where only a part of a cell is inside the damage zone (e.g., segment of a photoreceptor), it is unclear what minimally damaged fraction of a cell will result in acute cell death.

Computed and histological lesion diameter at the RPE was found to vary logarithmically with duration. Such dependence can be illustrated assuming a simple rectangular temperature pulse, which gives an Arrhenius integral,

$$\Omega \approx A\tau \exp\left(\frac{-E^*}{RT(r)}\right). \tag{10}$$

Assuming a constant Arrhenius integral value, this reduces to the condition: $T_o + \Delta T(r) \approx E^*/[R \ln(A\tau)]$, where $\Delta T(r)$ is the temperature rise and T_o is the initial temperature. For durations where heat diffusion from the irradiated area is significant, the computed temperature rise at the edge of the beam falls off as roughly $\Delta T \propto 1/r$ and increases linearly with power $\Delta T \propto P$. This gives a lesion radius r_L

$$r_L \propto r_0 + P\left[\frac{E^*}{R \ln(A\tau)} - T_o\right]^{-1}, \tag{11}$$

where r_0 is the beam diameter. This function is closely approximated by a logarithmic dependence on pulse duration in the millisecond range and linearly scales with power. Both trends are visible in Fig. 11(b) and have been previously reported for ophthalmoscopically measured lesion widths.[10]

5 Conclusions

A numerical model of retinal photocoagulation and rupture in rabbit has been established based on experimentally verified absorption properties. One of the essential features of the model is significant variability in RPE pigmentation. Lateral extent of tissue damage calculated with an Arrhenius activation energy of 340 kJ/mol matched histological findings. Calculated temperature at vaporization for pulse durations of $1-200$ ms was found to be approximately constant $(183 \pm 8\,^\circ\text{C})$.

The insight this model provides into the dynamics of retinal photocoagulation and rupture gives direction for future work toward maximizing the safe therapeutic window. For example, heat diffusion during the pulse results in an elevated temperature at the center of a conventional top-hat beam for durations of >1 ms. Such overheating results in a higher maximum temperature than necessary to produce the desired retinal coagulation and increases the probability of rupture. By choosing a ring-shaped beam with lower irradiance in the center, effects of thermal diffusion can be corrected, resulting in a more uniform temperature profile and Arrhenius contour. A beam shape that produces uniform heating in the treatment zone with no central overheating is expected to result in a wider therapeutic window and allow for shorter pulses to be used safely. In addition to allowing more exposures per treatment in scanning photocoagulation, reduced pulse duration would further improve the spatial confinement of the thermal effects in the retina. Future studies will use the model to cal-culate optimal beam parameters and the expected extent of improvement in the safety of photocoagulation in the millisecond range.

References

1. H. L. Little, H. C. Zweng, and R. R. Peabody, "Argon laser slit-lamp retinal photocoagulation," *Trans.-Am. Acad. Ophthalmol. Otolaryngol.* **74**(1), 85–97 (1970).
2. Early Treatment Diabetic Retinopathy Study Research Group, "Treatment techniques and clinical guidelines for photocoagulation of diabetic macular edema: Early Treatment Diabetic Retinopathy Study Report Number 2," *Ophthalmology* **94**(7), 761–774 (1987).
3. Macular Photocoagulation Study Group, "The influence of treatment extent on the visual acuity of eyes treated with Krypton laser for juxtafoveal choroidal neovascularization," *Arch. Ophthalmol. (Chicago)* **113**(2), 190–194 (1995).
4. N. S. Kapany, N. A. Peppers, H. C. Zweng, and M. Flocks, "Retinal photocoagulation by lasers," *Nature (London)* **199**, 146–149 (1963).
5. M. A. Mainster, "Decreasing retinal photocoagulation damage: principles and techniques," *Semin Ophthalmol.* **14**(4), 200–209 (1999).
6. M. S. Blumenkranz, D. Yellachich, D. E. Andersen, M. W. Wiltberger, D. Mordaunt, G. R. Marcellino, and D. Palanker, "Semiautomated patterned scanning laser for retinal photocoagulation," *Retina* **26**(3), 370–376 (2006).
7. S. Al-Hussainy, P. M. Dodson, and J. M. Gibson, "Pain response and follow-up of patients undergoing panretinal laser photocoagulation with reduced exposure times," *Eye* **22**(1), 96–99 (2008).
8. J. Roider, F. Hillenkamp, T. Flotte, and R. Birngruber, "Microphotocoagulation—selective effects of repetitive short laser-pulses," *Proc. Natl. Acad. Sci. U.S.A.* **90**(18), 8643–8647 (1993).
9. A. Obana, "The therapeutic range of chorioretinal photocoagulation with diode and argon lasers: an experimental comparison," *Lasers Light Ophthalmol.* **4**(3/4), 147–156 (1992).
10. A. Jain, M. S. Blumenkranz, Y. Paulus, M. W. Wiltberger, D. E. Andersen, P. Huie, and D. Palanker, "Effect of pulse duration on size and character of the lesion in retinal photocoagulation," *Arch. Ophthalmol. (Chicago)* **126**(1), 78–85 (2008).
11. S. Schmidt and R. Peisch, "Melanin concentration in normal human retinal pigment epithelium. regional variation and age-related reduction," *Invest. Ophthalmol. Visual Sci.* **27**(7), 1063–1067 (1986).
12. J. Weiter, F. Delori, G. Wing, and K. Fitch, "Retinal pigment epithelial lipofuscin and melanin and choroidal melanin in human eyes," *Invest. Ophthalmol. Visual Sci.* **27**(2), 145–152 (1986).
13. K. Schulmeister, J. Husinsky, B. Seiser, F. Edthofer, H. Tuschl, and D. J. Lund, "Ex-plant retinal laser induced threshold studies in the millisecond time regime," *Proc. SPIE* **6084**, 60841E (2006).
14. A. J. Welch, "The Thermal Response of Laser Irradiated Tissue," *IEEE J. Quantum Electron.* **20**(12), 1471–1481 (1984).
15. R. Birngruber, F. Hillenkamp, and V. P. Gabel, "Theoretical investigations of laser thermal retinal injury," *Health Phys.* **48**(6), 781–796 (1985).
16. J. Sandeau, G. Caillibotte, J. Kandulla, R. Birngruber, and G. Apiou-Sbirlea, "Modeling of conductive and convective heat transfers in retinal laser treatments," *Proc. SPIE* **6131**, 61381A (2006).
17. C. R. Thompson, B. S. Gerstman, S. L. Jacques, and M. E. Rogers, "Melanin granule model for laser-induced thermal damage in the retina," *Bull. Math. Biol.* **58**(3), 513–553 (1996).

18. R. K. Banerjee, L. Zhu, P. Gopalakrishnan, and M. J. Kazmierczak, "Influence of laser parameters on selective retinal treatment using single-phase heat transfer analyses," *Med. Phys.* **34**(5), 1828–1841 (2007).

19. F. C. Henriques and A. R. Moritz, "Studies of thermal injury in the conduction of heat to and through skin and the temperatures attained therein—a theoretical and an experimental investigation," *Am. J. Pathol.* **23**(4), 915–934 (1947).

20. J. P. a. S. Thomsen, "Rate process analysis of thermal damage," in *Optical-Thermal Response of Laser-Irradiated Tissue*, A. J. W. a. M. J. C. v. Gemert, Ed., pp. 561–603, Plenum, New York (1995).

21. G. Schuele, M. Rumohr, G. Huettmann, and R. Brinkmann, "RPE damage thresholds and mechanisms for laser exposure in the microsecond-to-millisecond time regimen," *Invest. Ophthalmol. Visual Sci.* **46**(2), 714–719 (2005).

22. R. Brinkmann, G. Huttmann, J. Rogener, J. Roider, R. Birngruber, and C. P. Lin, "Origin of retinal pigment epithelium cell damage by pulsed laser irradiance in the nanosecond to microsecond time regimen," *Lasers Surg. Med.* **27**(5), 451–464 (2000).

23. P. W. Lappin and P. S. Coogan, "Relative sensitivity of various areas of the retina to laser radiation," *Arch. Ophthalmol. (Chicago)* **84**(3), 350–354 (1970).

24. M. Niemz, *Laser-Tissue Interactions. Fundamentals and Applications*, Springer, Berlin (2002).

25. D. M. Simanovskii, M. A. Mackanos, A. R. Irani, C. E. O'Connell-Rodwell, C. H. Contag, H. A. Schwettman, and D. V. Palanker, "Cellular tolerance to pulsed hyperthermia," *Phys. Rev. E* **74**(1 Pt 1), 011915 (2006).

26. S. Bhowmick, J. E. Coad, D. J. Swanlund, and J. C. Bischof, "In vitro thermal therapy of AT-1 Dunning prostate tumours," *Int. J. Hyperthermia* **20**, 73–92 (2004).

27. J. R. Lepock, "Cellular effects of hyperthermia: relevance to the minimum dose for thermal damage," *Int. J. Hyperthermia* **19**, 252–266 (2003).

28. J. Kampmeier, B. Radt, R. Birngruber, and R. Brinkmann, "Thermal and biomechanical parameters of porcine cornea," *Cornea* **19**(3), 355–363 (2000).

29. A. Z. Vassiliadis, H. Christian, and K. G. Dedrick, "Ocular laser threshold investigations," in SRI Proj. No. 8209, Stanford Research Institute, Menlo Park, CA (1971).

30. W. Rasband, "ImageJ," U. S. National Institute of Health, Bethesda, MD (2004).

31. R. Birngruber, E. Drechsel, F. Hillenkamp, and V.-P. Gabel, "Minimal spot size on the retina formed by the optical system of the eye," *Int. Ophthalmol.* **1**(3), 175–178 (1979).

32. R. Birngruber, "Choroidal circulation and heat convection at the fundus of the eye: implications for laser coagulation and the stabilization of retinal temperature," in *Laser Applications to Medicine and Biology*, M. L. Wolbarsht, Ed., pp. 277–361, Plenum Press, London (1991).

33. Invitrogen, LIVE/DEAD (R) Viability/Cytotoxicity Kit, Data Sheet, ⟨http://www.invitrogen.com/⟩ (2005).

34. "COMSOL Multiphysics 3.4," COMSOL Inc. ⟨http://www.comsol.com/⟩ (2007).

35. "Revised Release on the IAPS Formulation 1985 for the Thermal Conductivity of Ordinary Water Substance for General and Scientific Use," Int. Assoc. for Properties of Water and Steam (1998).

36. A. J. Welch, E. H. Wissler, and L. A. Priebe, "Significance of blood-flow in calculations of temperature in laser irradiated tissue," *IEEE Trans. Biomed. Eng.* **27**(3), 164–166 (1980).

37. M. J. C. Vangemert and J. P. H. Henning, "A model approach to laser coagulation of dermal vascular-lesions," *Arch. Dermatol. Res.* **270**(4), 429–439 (1981).

38. P. Kubelka, "New contributions to the optics of intensely light-scattering materials 1.," *J. Opt. Soc. Am.* **38**(5), 448–457 (1948).

39. M. Hammer, A. Roggan, D. Schweitzer, and G. Muller, "Optical properties of ocular fundus tissues—an *in vitro* study using the double-integrating-sphere technique and inverse Monte Carlo simulation," *Phys. Med. Biol.* **40**(6), 963–978 (1995).

40. S. L. Jacques, "Role of tissue optics and pulse duration on tissue effects during high-power laser irradiation," *Appl. Opt.* **32**(13), 2447–2454 (1993).

41. G. Schule, G. Huttmann, C. Framme, J. Roider, and R. Brinkmann, "Noninvasive optoacoustic temperature determination at the fundus of the eye during laser irradiation," *J. Biomed. Opt.* **9**(1), 173–179 (2004).

42. J. S. Pollack, J. E. Kim, J. S. Pulido, and J. M. Burke, "Tissue effects of subclinical diode laser treatment of the retina 10.1001/archopht.116.12.1633," *Arch. Ophthalmol. (Chicago)* **116**(12), 1633–1639 (1998).

43. V. P. Gabel, R. Birngruber, and F. Hillenkamp, "Visible and near infrared light absorption in pigment epithelium and choroid.," Congress Series: XXIII Concilium Ophthalmologicum **450**, 658–662 (1978).

44. M. F. Marmor and T. J. Wolfensberger, *The Retinal Pigment Epithelium: Function and Disease*, Oxford University Press, London (1998).

45. R. Brinkmann, J. Roegener, C. P. Lin, J. Roider, R. Birngruber, and G. Huettmann, "Selective RPE photodestruction: mechanism of cell damage by pulsed-laser irradiance in the ns to mu m time regime," *Proc. SPIE* **3601**, 59–65 (1999).

46. H. Lee, C. Alt, C. M. Pitsillides, and C. P. Lin, "Optical detection of intracellular cavitation during selective laser targeting of the retinal pigment epithelium: dependence of cell death mechanism on pulse duration," *J. Biomed. Opt.* **12**(6), 064034 (2007).

47. J. Roegener, R. Brinkmann, and C. P. Lin, "Pump-probe detection of laser-induced microbubble formation in retinal pigment epithelium cells," *J. Biomed. Opt.* **9**(2), 367–371 (2004).

48. J. Neumann and R. Brinkmann, "Boiling nucleation on melanosomes and microbeads transiently heated by nanosecond and microsecond laser pulses," *J. Biomed. Opt.* **10**(2), 024001 (2005).

49. J. Li, G. P. Peterson, and P. Cheng, "Dynamic characteristics of transient boiling on a square platinum microheater under millisecond pulsed heating," *Int. J. Heat Mass Transfer* **51**(1–2), 273–282 (2008).

50. H. S. Carlsaw and J. C. Jaeger, *Conduction of Heat in Solids*, Oxford University Press, London (1959).

51. T. P. Kidwell, L. A. Priebe, and A. J. Welch, "Measurement of ocular transmittance and irradiation distribution in argon-laser irradiated rabbit eyes," *Invest. Ophthalmol.* **15**(8), 668–671 (1976).

52. L. A. Priebe, C. P. Cain, and A. J. Welch, "Temperature rise required for production of minimal lesions in macaca-mulatta retina," *Am. J. Ophthalmol.* **79**(3), 405–413 (1975).

53. W. Weinberg, R. Birngruber, and B. Lorenz, "The change in light reflection of the retina during therapeutic laser photocoagulation," *IEEE J. Quantum Electron.* **20**(12), 1481–1489 (1984).